

PROCEEDINGS A

rspa.royalsocietypublishing.org

Research



Article submitted to journal

Subject Areas:

machine learning, signal processing

Keywords:

Gaussian processes, deconvolution, Bayesian inference

Author for correspondence:

Felipe Tobar

e-mail: ftobar@uchile.clGaussian Process
DeconvolutionFelipe Tobar¹, Arnaud Robert² and Jorge
F. Silva³¹Initiative for Data & Artificial Intelligence, Universidad de Chile²Department of Computing, Imperial College London³Department of Electrical and Electronic Engineering, Universidad de Chile

Let us consider the deconvolution problem, that is, to recover a latent source $x(\cdot)$ from the observations $\mathbf{y} = [y_1, \dots, y_N]$ of a convolution process $y = x \star h + \eta$, where η is an additive noise, the observations in \mathbf{y} might have missing parts with respect to y , and the filter h could be unknown. We propose a novel strategy to address this task when x is a continuous-time signal: we adopt a Gaussian process (GP) prior on the source x , which allows for closed-form Bayesian nonparametric deconvolution. We first analyse the direct model to establish the conditions under which the model is well defined. Then, we turn to the inverse problem, where we study i) some necessary conditions under which Bayesian deconvolution is feasible, and ii) to which extent the filter h can be learnt from data or approximated for the blind deconvolution case. The proposed approach, termed Gaussian process deconvolution (GPDC) is compared to other deconvolution methods conceptually, via illustrative examples, and using real-world datasets.

This is the author generated postprint of the accepted manuscript (i.e., the accepted version not typeset by the journal) produced to be shared in personal or public repositories.

1. Introduction

In signal processing, the convolution between a (continuous-time) source x and a filter h , denoted by¹

$$f(t) = x \star h = \int_{\mathbb{R}} x(\tau)h(t - \tau)d\tau, \quad (1.1)$$

can be understood as a generalised (noiseless) observation of x through an acquisition device with impulse response h . Here, h reflects the quality or precision of the observation device, since the "closer" h is to a Dirac delta, the "closer" the convolved quantity f is to the source x .

This convolution model, and the need to recover the source signal x from a set of noisy observations of f , arise in a number of scenarios including: astronomy [1], channel equalisation in telecommunications [2], de-reverberation [3], seismic wave reconstruction [4], and image restoration [5] to name a few. In these scenarios, practitioners need to remove the unwanted artefacts introduced by the non-ideal filter h , in other words, they require to perform a *deconvolution* to recover x from f . In practice, the deconvolution operates over observations that are noise-corrupted (due to sensing procedure) realisations of f , denoted y in our setting. Furthermore, we will *de facto* assume that there are missing observations, since our formulation establishes the source x and the convolution f as continuous-time objects while the observations y are always finite meaning that there are "missing parts" in the observations. Fig. 1 illustrates this procedure for the image of a bird using the proposed method.

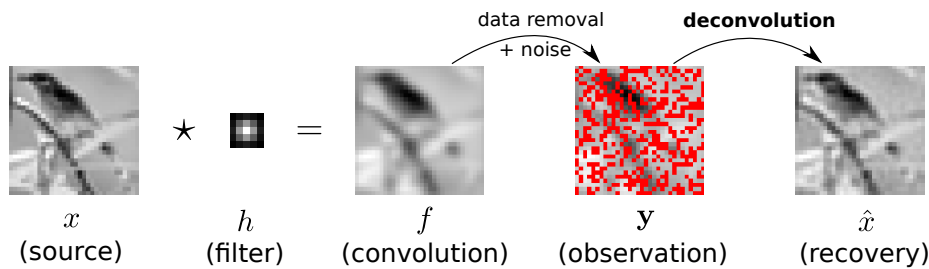


Figure 1: Illustration of the deconvolution operation: an image x is convolved with a filter h to produce the blurry image f , which is then corrupted (additive noise and data removal in red) to yield y . Deconvolution aims to produce an estimator of the original signal x from y denoted \hat{x} . This image produced by the proposed method.

As a particular instance of inverse problems, the deconvolution of corrupted signals has been largely addressed from a statistical perspective [6–8]. This approach is intimately related to the linear filter theory, where the foundations laid by the likes of [9,10] are still at the core of modern-day implementations of deconvolution. A common finding across the vast deconvolution literature is that, under the presence of noisy or missing data, an adequate model for reconstructing f (from y) before the deconvolution is fundamental. From a Bayesian perspective, this boils down to an appropriate choice of the prior distribution of the source x ; we proceed by imposing a Gaussian process prior on the source.

(a) Contribution and organisation

Despite the ubiquity of the deconvolution problem and the attention it has received [11], we claim that the recovery of continuous-time signals from a finite number of corrupted (convolved) samples from a Bayesian standpoint, **which can provide error bars for the deconvolution**, has been largely underexplored. With this challenge in mind, we study Bayesian nonparametric

¹For a lighter notation, we use the compact expressions x , h and f to represent the functions $(x(t))_{t \in \mathbb{R}}$, $(h(t))_{t \in \mathbb{R}}$, and $(f(t))_{t \in \mathbb{R}}$ respectively.

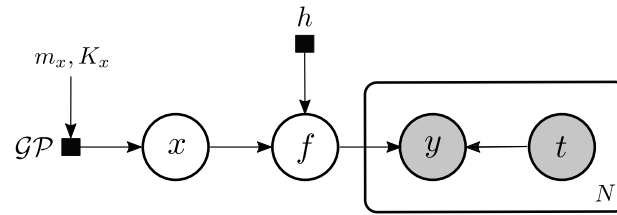


Figure 2: Graphical model for the hierarchical GP convolution. Recall that observed and latent random variables are shown in grey and white circles respectively, while black squares denote fixed parameters.

deconvolution using a Gaussian process (GP) prior over the latent source x , our method is thus termed Gaussian process deconvolution (GPDC). The main contributions of our work include: i) the conditions for the proposed model to be well defined and how to generate samples from it; ii) the closed-form solution for the posterior deconvolution and when this deconvolution is possible; iii) its application to the blind deconvolution and the required approximations; and iv) experimental validation of our GPDC method on 1D and 2D real-world data.

The article is organised as follows. Sec. 2 presents the convolution as a GP hierarchical model and the related literature. Sec. 3 studies the *direct model* (i.e., x generates f and y) and defines the requirements of $h(t)$ and x for $f(t)$ to be well defined point-wise. Then, Sec. 4 focuses on the *inverse problem* (i.e., x is estimated from y) and studies the recovery from the Fourier representation perspective. Sec. 5 addresses the blind deconvolution (i.e., h is unknown), while Secs. 6 and 7 present the experimental validation and conclusions respectively.

2. Deconvolution using GPs

(a) Proposed generative model

Let us consider the following hierarchical model (see Fig. 2 for the graphical representation):

$$\text{source process: } x(t) \sim \mathcal{GP}(m_x(t), K_x(t)), \quad (2.1)$$

$$\text{convolution: } f(t) = \int_{\mathbb{R}} x(\tau)h(\tau - t)d\tau, \quad (2.2)$$

$$\text{observations: } y_i \sim \mathcal{N}(f(t_i), \sigma_n^2), i = 1, \dots, N, \quad (2.3)$$

where $\mathbf{t} = \{t_i\}_{i=1}^N \in \mathbb{R}^N$ indicate the observation times. First, eq. (2.1) places a stationary GP prior on the source with covariance $K_x(t)$; we will assume $m_x(t) = 0$ for all t . This selection follows the rationale that the prior distribution is key for implementing deconvolution under missing and noisy data, and the well-known interpolation properties of GPs [12]. Second, eq. (2.2) defines the continuous-time convolution process f through a linear and time-invariant filter h . Third, eq. (2.3) defines a Gaussian likelihood, where the noisy observations of f at times \mathbf{t} are denoted by $\mathbf{y} = [y_1, \dots, y_N] \in \mathbb{R}^N$. Notice that the observations \mathbf{y} only see "parts" of $f(\cdot)$ and thus a Bayesian approach is desired to quantify the uncertainty related to the conditional process $x|\mathbf{y}$.

(b) Relationship to classical methods and prior work

Perhaps the simplest approaches to deconvolution are the *Inverse FT* method, which performs deconvolution as a point-wise division between Fourier transforms $\mathcal{F}^{-1}\{\mathcal{F}\{\mathbf{y}\}/\mathcal{F}\{\mathbf{h}\}\}$ — where \mathbf{h} is a discrete version of the filter h — and the *Wiener method*, which finds the optimal estimate of x in the mean-square-error sense. Both methods assume a known filter and perform a division in the Fourier domain which can be unstable in practice. The first Bayesian take on the deconvolution problem can be attributed to Bretthorst in 1992, who proposed to use

a multivariate normal (MVN) prior for the discrete-time case [13]. A year later, Rhode and Whittenburg addressed the Bayesian deconvolution of exponentially-decaying sinewaves [14], and then Sir David Mackay's book presented the Bayesian derivation of the deconvolution problem assuming an MVN prior and connects it to other methods with emphasis on image restoration [15, Ch. 46]. In the Statistics community, deconvolution refers to the case when x and h are probability densities rather than time series; this case is beyond our scope.

The use of different priors for Bayesian deconvolution follows the need to cater for specific properties of the latent time series x . For instance, [16] considered a mixture of Laplace priors which required variational approximations, while [17] implemented a total variation prior with the aim of developing reliable reconstruction of images. However, little attention has been paid, so far, to the case when the source x is a continuous time signal. Most existing approaches assume priors only for discrete-time finite sequences (or vectors) and, even though they can still be applied to continuous data by quantising time, their computational complexity explodes for unevenly sampled data or dense temporal grids. In the same manner, the kriging literature, which is usually compared to that of GPs, has addressed the deconvolution problem (see, e.g., [18,19]) but has not yet addressed the continuous-time setting from a probabilistic perspective. Additionally, recent advances of deconvolution in the machine learning and computer vision communities mainly focus on blending neural networks models with classic concepts such as prior design [20] and the Wiener filter [21], while still considering discrete objects (not continuous time) and not allowing in general for missing data.

Convolution models have been adopted by the GP community mainly to parametrise covariance functions for the multioutput [22–24] and non-parametric cases [25,26]. With the advent of deep learning, researchers have replicated the convolutional structure of convolutional NNs (CNNs) on GPs. For instance, Deep Kernel Learning (DKL) [27] concatenates a CNN and a GP so that the kernel of the resulting structure—also a GP—sports *shared weights and biases*, which are useful for detecting common features in different regions of an image and provides robustness to translation of objects. Another example are convolutional GPs [28], which extend DKL by concatenating the kernel with a *patch-response function* that equips the kernel with convolutional structure without introducing additional hyperparameters. This concept has been extended to graphs and deep GPs—see [29,30] respectively.

Though convolutions have largely aided the design of kernels for GPs, contributions in the "opposite direction", that is, to use the GP toolbox as a means to address the general deconvolution problem, are scarce. To the best of our knowledge, the only attempts to perform Bayesian deconvolution using a GP prior are works that either: focus specifically in detecting magnetic signals from spectropolarimetric observations [31]; only consider discrete-time impulse responses [32]; or, more recently, use an MVN prior for the particular case of a non-stationary Matérn covariance [33], a parametrisation proposed by [34] which has, in particular, been used for scatter radar data [35].

Building on the experimental findings of these works implementing deconvolution using GPs, our work focuses on the analysis and study of kernels and filters, in terms of their ability to recover $x(t)$ from y . The proposed strategy, termed GPDC, is expected to have superior modelling capabilities as compared to previous approaches, while having a closed form posterior deconvolution density which is straightforward to compute. However, there are aspects to be addressed before implementing GPDC, these are: i) when the integral in eq. (2.2) is finite in terms of the law of x , ii) when x can be recovered from y , iii) how the blind scenario can be approached. Addressing these questions are the focus of the following sections.

3. Analysis of the direct model

(a) Assumptions on x and h , and their impact on f

We assume that x is a stationary GP and its covariance kernel K_x is integrable (i.e., $K_x \in L_1$); this is needed for x to have a well-defined Fourier power spectral density (PSD). Additionally,

although the sample paths x are in general not integrable, they are *locally integrable* due to $K_x \in L_1$, therefore, we assume that the filter h decays *fast enough* such that the integral in eq. (2.2) is finite. This is always obtained when either h has compact support or when it is dominated by a Laplacian or a Square Exponential function. If these properties (integrability and stationarity) are met for x , they translate to f via the following results.

Remark 1. If $f(t)$ in eq. (2.2) is finite point-wise for any $t \in \mathbb{R}$, then $f(t) \sim \mathcal{GP}(0, K_f(t))$ with stationary kernel

$$K_f(t) = \int_{\mathbb{R}^2} h(\tau')h(\tau)K_x(\tau - (\tau' - t))d\tau d\tau'. \quad (3.1)$$

Lemma 1. If the convolution filter h and the covariance K_x are both integrable, then K_f in eq. (3.1) is integrable.

Proof. The integrability of $K_f(t)$ in eq. (3.1) follows directly from applying Fubini Theorem and the triangle inequality (twice) to $\int_{\mathbb{R}} |K_f(t)|dt$, to obtain $\int_{\mathbb{R}} |K_f(t)|dt < \infty$ (full proof in the Appendix). \square

Remark 2. Lemma 2 provides a **sufficient** condition for the integrability of K_f , thus theoretically justifying i) a Fourier-based analysis of f , and ii) relying upon the GP machinery to address deconvolution from the lens of Bayesian inference. However, the conditions in Lemma 2 are **not necessary**; for instance, if the filter h is the (non-integrable) Sinc function, the generative model in eqs. (2.1)-(2.3) is still well defined (see Example 2).

(b) Sampling from the convolution model

We devise two ways of sampling from f in eq. (2.2): we could either i) draw a path from $x \sim \mathcal{GP}(0, K_x(t))$ and convolve it against h , or ii) sample directly from $f \sim \mathcal{GP}(0, K_f(t))$. However, both alternatives have serious limitations. The first one cannot be implemented numerically since the convolution structure implies that every element in f depends on infinite values of x (for a general h). The second alternative bypasses this difficulty by directly sampling a finite version of f , however, by doing so x is integrated out, meaning that we do not know "to which" sample trajectory of x the (finite) samples of f correspond.

The key to jointly sample finite versions (aka *marginalisations*) of the source and convolution processes lies on the fact that, although the relationship between x and f established by eq. (2.2) is deterministic, the relationship between their finite versions becomes stochastic. Let us denote² finite versions of x and f by $\mathbf{x} = x(\mathbf{t}_x)$ and $\mathbf{f} = f(\mathbf{t}_f)$ respectively, where $\mathbf{t}_x \in \mathbb{R}^{N_x}$ and $\mathbf{t}_f \in \mathbb{R}^{N_f}$. Therefore, we can hierarchically sample according to $p(\mathbf{x}, \mathbf{f}) = p(\mathbf{f}|\mathbf{x})p(\mathbf{x})$ in two stages: we first sample $\mathbf{x} \sim \text{MVN}(0, K_x(\mathbf{t}_x))$ and then $\mathbf{f}|\mathbf{x} \sim p(\mathbf{f}|\mathbf{x})$ given by³

$$\begin{aligned} p(\mathbf{f}|\mathbf{x}) &= \text{MVN}\left(\mu_{\mathbf{f}|\mathbf{x}}, \sigma_{\mathbf{f}|\mathbf{x}}^2\right) \\ \mu_{\mathbf{f}|\mathbf{x}} &= K_{fx}(\mathbf{t}_f, \mathbf{t}_x)K_x^{-1}(\mathbf{t}_x)\mathbf{x} \\ \sigma_{\mathbf{f}|\mathbf{x}}^2 &= K_f(\mathbf{t}_f) - K_{fx}(\mathbf{t}_f, \mathbf{t}_x)K_x^{-1}(\mathbf{t}_x)K_{xf}(\mathbf{t}_x, \mathbf{t}_f), \end{aligned} \quad (3.2)$$

where $K_{fx}(t_1, t_2) = K_{fx}(t_1 - t_2)$ is the stationary covariance between f and x , given element-wise by

$$K_{fx}(t_1, t_2) = K_{fx}(t_1 - t_2) = \int_{\mathbb{R}} h(t - (t_1 - t_2))K_x(t)dt. \quad (3.3)$$

The integrability of K_{fx} in eq. (3.3) is obtained similarly to that of K_f in Lemma 2, under the assumption that $h, K_x \in L_1$.

²Here, we use the compact notation $x(\mathbf{t}) = [x(t_1), \dots, x(t_n)]$, where $\mathbf{t} = [t_1, \dots, t_n]$.

³We use the reversed-argument notation $K_{xf}(\mathbf{t}_x, \mathbf{t}_f) = K_{fx}^T(\mathbf{t}_f, \mathbf{t}_x)$ to avoid the use of transposes.

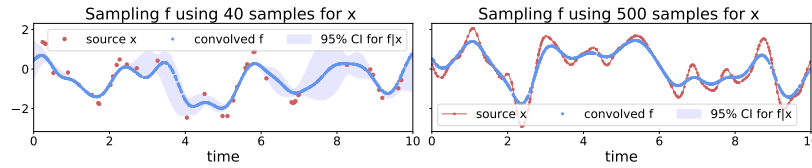


Figure 3: Hierarchical sampling \mathbf{x} and \mathbf{f} considering 40 (left) and 500 (right) samples for \mathbf{x} in the interval $[0,10]$. Both K_x and h (and consequently K_{x_f} and K_f) are square-exponential kernels with lengthscale $l = \sqrt{0.05}$ (rate $\gamma = 10$).

Furthermore, let us recall that the conditional mean of $f(t)|\mathbf{x}$ is given by

$$\mathbb{E}[f(t)|\mathbf{x}] = \int_{\mathbb{R}} h(t + \tau) \mathbb{E}[x(\tau)|\mathbf{x}] d\tau. \quad (3.4)$$

This expression reveals that the expected value of $f(t)$ given \mathbf{x} can be computed by first calculating the average interpolation of x given \mathbf{x} , denoted $\mathbb{E}[x(\tau)|\mathbf{x}]$, and then applying the convolution to this interpolation as per eq. (2.2).

Additionally, let us also recall that the conditional variance of $f(t)|\mathbf{x}$ is given by

$$\mathbb{V}[f(t)|\mathbf{x}] = \int_{\mathbb{R}^2} h(t + \tau) \mathbb{V}[x(\tau), x(\tau')|\mathbf{x}] h(t + \tau') d\tau d\tau'.$$

Observe that since the posterior variance of a GP decreases with the amount of observations, $\mathbb{V}[x(\tau), x(\tau')|\mathbf{x}]$ approaches zero whenever \mathbf{t}_x become more dense, and consequently so does $\mathbb{V}[f(t)|\mathbf{x}]$. Therefore, the more elements in \mathbf{x} , the smaller the variance $\mathbb{V}[f(t)|\mathbf{x}]$ and thus the trajectories of $f|\mathbf{x}$ become concentrated around the posterior mean in eq. (3.4). This resembles a connection with the discrete convolution under missing source data, where one "interpolates and convolves", emphasising the importance of the interpolation (i.e., the prior) of x . Definition 1 presents the Square Exponential (SE) kernel, and then Example 1 illustrates the sampling procedure and the concentration of $f|\mathbf{x}$ around its mean.

Definition 1. *The stationary kernel defined as*

$$K_{SE}(t) = \sigma^2 \exp\left(-\frac{1}{2l^2}t^2\right) \quad (3.5)$$

is referred to as Square Exponential (SE) and its parameters are magnitude σ and lengthscale l . Alternatively, the SE kernel's lengthscale can be defined in terms of its inverse lengthscale (or rate) $\gamma = \frac{1}{2l^2}$. The Fourier transform of the SE kernel is also an SE kernel, therefore, the support of the PSD of a GP with the SE kernel is the entire real line.

Example 1. *Let us consider K_x and h to be SE kernels with lengthscale $l = \sqrt{0.05}$ (rate $\gamma = 10$), thus, K_f and K_{x_f} are SE as well. Fig. 3 shows \mathbf{x} and \mathbf{f} sampled over the interval $t \in [0, 10]$: at the left (resp. right) plot, we sampled a 40-dimensional (resp. 500-dimensional) vector \mathbf{x} shown in red to produce a 1000-dimensional vector \mathbf{f} shown in blue alongside the 95% error bars for $p(f(t)|\mathbf{x})$ in both plots. Notice how the larger dimensionality of \mathbf{x} over the fixed interval resulted in a tighter conditional density $p(f(t)|\mathbf{x})$.*

Remark 3. *The GP representation of the convolution process allows us to generate finite samples \mathbf{x} , \mathbf{f} (over arbitrary inputs) of the infinite-dimensional processes x and f respectively. This represents a continuous and probabilistic counterpart to the classic discrete-time convolution that i) can be implemented computationally and, ii) is suitable for real-world scenarios where data may be non-uniformly sampled.*

4. The inverse problem: Bayesian nonparametric deconvolution

We now turn to the inverse problem of recovering x from the finite vector $\mathbf{y} = [y_1, \dots, y_N]$ observed at times $\mathbf{t} = [t_1, \dots, t_N]$. In our setting defined in eqs. (2.1)-(2.3), the deconvolution $x|\mathbf{y}$ is a GP given by

$$x|\mathbf{y} \sim \mathcal{GP}(\mu, \sigma^2) \quad (4.1)$$

$$\mu(t) = K_{xy}(t, \mathbf{t})K_{\mathbf{y}}^{-1}\mathbf{y}, \quad (4.2)$$

$$\sigma^2(t_1, t_2) = K_x(t_1, t_2) - K_{xy}(t_1, \mathbf{t})K_{\mathbf{y}}^{-1}K_{yx}(\mathbf{t}, t_2), \quad (4.3)$$

where $K_{\mathbf{y}} = K_f(\mathbf{t}, \mathbf{t}) + \mathbf{I}_N\sigma_n^2$ is the marginal covariance matrix of the observations vector \mathbf{y} , \mathbf{I}_N is the N -size identity matrix, and $K_{xy}(t_1, t_2)$ denotes the cross-covariance between $x(t_1)$ and $y(t_2)$, which is in turn equal to $K_{xf}(t_1, t_2) = K_{xf}(t_1 - t_2)$.

(a) When is deconvolution possible?

We aim to identify the circumstances under which \mathbf{y} provides *enough information* to determine x with as little uncertainty as possible. To this end, we consider a windowed (Fourier) spectral representation of $x|\mathbf{y}$ —the GP in eq.(4.1)—given by

$$\hat{x}_w(\xi) = \mathcal{F}\{w(t)x(t)\}(\xi) = \int_{\mathbb{R}} w(t)x(t)e^{-j2\pi\xi t} dt, \quad (4.4)$$

where $\mathcal{F}\{\cdot\}$ denotes the continuous-time Fourier transform (FT) operator, $\xi \in \mathbb{R}$ is the frequency variable, and the window $w: \mathbb{R} \rightarrow \mathbb{R}$ has compact support (such that the integral above is finite). This windowed spectral representation is chosen since the GP $x|\mathbf{y}$ is nonstationary (its power spectral density is not defined), and the sample trajectories of $x|\mathbf{y}$ following the distribution $\mathcal{GP}(\mu, \sigma^2)$ are not Lebesgue integrable in general (their FT cannot be computed). Based on the representation introduced in eq. (4.4), we define the concept of *successful recovery* and link it to the spectral representation of K_x and h .

Definition 2. We say that $x(\cdot)$ can be *successfully recovered* from observations $\mathbf{y} = [y_1, \dots, y_N]$ if, $\forall \xi \in \mathbb{R}$, the spectral representation $\hat{x}_w(\xi)$ in eq. (4.4) can be recovered at an arbitrary precision by increasing the amount of observations N , for an arbitrary compact-support window $w(\cdot)$.

Theorem 1. For the setting defined in eqs. (2.1)-(2.3), a necessary condition to successfully recover x from \mathbf{y} is that the spectral support of h contains that of K_x , that is, $\text{supp } \mathcal{F}\{K_x\} \subseteq \text{supp } \mathcal{F}\{h\}$.

Proof. From eqs. (2.1)-(2.3) and linearity of the FT, the windowed spectrum $\hat{x}_w(\xi)$ is given by a complex-valued⁴ GP, with mean and marginal variance (calculations in the Appendix):

$$\mu_{\hat{x}_w}(\xi) = \left(\hat{m}_x(\xi) + \hat{K}_x(\xi)\hat{h}(\xi)e^{-j2\pi\xi\mathbf{t}}K_{\mathbf{y}}^{-1}\mathbf{y} \right) \star \hat{w}(\xi), \quad (4.5)$$

$$\begin{aligned} \sigma_{\hat{x}_w}^2(\xi) &= \hat{K}_x(\xi) \star |\hat{w}(\xi)|^2 \\ &\quad - \|\hat{w}(\xi) \star \hat{K}_x(\xi)\hat{h}(\xi)e^{-j2\pi\xi\mathbf{t}}\|_{K_{\mathbf{y}}^{-1}}, \end{aligned} \quad (4.6)$$

where $\|\mathbf{v}\|_A = \mathbf{v}^\top A \mathbf{v}$ denotes the Mahalanobis norm of \mathbf{v} w.r.t. matrix A , and $\hat{h} = \mathcal{F}\{h\}$ was used as a compact notation for the FT of h . Following Definition 2, successful recovery is achieved when the posterior variance of $\hat{x}_w(\xi)$ vanishes, i.e., when the two terms at the right hand side of eq. (4.6) cancel one another. For this to occur, it is necessary that these terms have the same support, however, as this should happen for an arbitrary window $\hat{w}(\xi)$ we require that $\text{supp } \hat{K}_x(\xi) = \cup_{i=1}^N \text{supp } \hat{K}_x(\xi)\hat{h}(\xi)e^{-j2\pi\xi t_i}$. Since $\cup_{i=1}^N \text{supp } e^{-j2\pi\xi t_i} = \mathbb{R}$, what is truly needed is that $\text{supp } \hat{K}_x(\xi) = \text{supp } \hat{K}_x(\xi)\hat{h}(\xi)$ which is obtained when $\text{supp } \hat{K}_x(\xi) \subseteq \text{supp } \hat{h}(\xi)$. \square

⁴For complex-valued GPs, see [36–38].

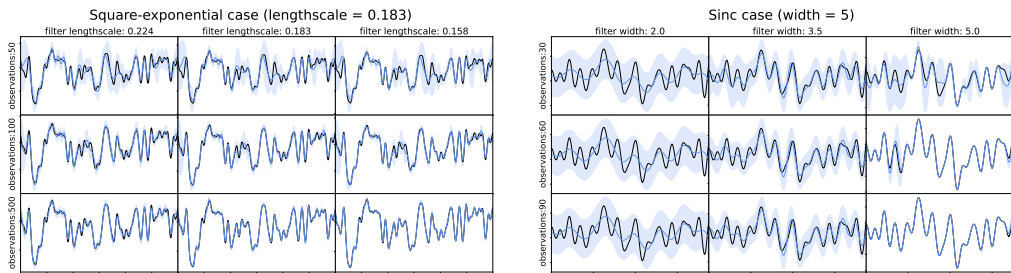


Figure 4: Implementation of GPDC when both h and K_x are SE (left) or Sinc (right). In each case, we considered increasing number of observations \mathbf{y} (top to bottom) and different parameters for h (left to right)— the values for all the width and lengthscale parameters are presented in the figure titles. The plots show the ground truth source x (black), the posterior GPDC deconvolution mean (blue) and GPDC's 95% error bars (light blue). In line with Theorem 1 and Remark 4, notice how in the SE case (left) more observations improve the recovery, whereas in the Sinc case (right) recovery is not possible even for increasing amount of observations when the filter is too narrow (first and second columns).

Remark 4. Theorem 1 gives a *necessary* condition to recover x from \mathbf{y} in terms of how much of the spectral content of x , represented by \hat{K}_x , is not suppressed during the convolution against h and thus can be extracted from \mathbf{y} . A stronger *sufficient* condition for successful recovery certainly depends on the locations where \mathbf{y} is measured. Intuitively, recovery depends on having enough observations, and on the vector $e^{-j2\pi\xi\mathbf{t}}$ being aligned with the eigenvectors of $K_y^{-1}(\mathbf{t}, \mathbf{t})$ defining the norm in eq. (4.6); thus resembling the sampling theorem in [39,40].

Definition 3 introduces the Sinc kernel [41]. Then, Example 2 illustrates the claims in Theorem 1 and Remark 4, where GPDC recovery is assessed in terms of spectral supports and amount of observations.

Definition 3. The stationary kernel defined as

$$K_{\text{Sinc}}(t) = \frac{\sigma^2 \sin(\Delta\pi t)}{\Delta\pi t} \quad (4.7)$$

is referred to as the (centred) Sinc kernel and its parameters are magnitude σ and width Δ . Though the Sinc function is not integrable (see Lemma 2), it admits a Fourier transform which takes the form of a rectangle of width Δ centred in zero. Therefore, a GP with a Sinc kernel does not generate paths with frequencies greater than $\Delta/2$.

Example 2. Let us consider two scenarios for GPDC: In the first one, both K_x and h are Square Exponential (SE) kernels and therefore $\text{supp } \mathcal{F}\{K_x\} = \text{supp } \mathcal{F}\{h\} = \mathbb{R}$. In the second case, both K_x and h are Sinc kernels [41], and the overlap of their PSDs depends on their parameters. We implemented GPDC in both cases for different amount of observations and parameters, in particular, we considered the scenario where $\text{supp } \hat{K}_x \not\subset \text{supp } \hat{h}$ for the Sinc case. Fig. 4 (left) shows how in the SE case an increasing number of observations always improves the recovery regardless of the parameters of h and K_x . On the contrary, notice that for the Sinc case (Fig. 4, right), even with a large number of observations, the latent source x cannot be recovered. This is due to certain spectral components of x being removed by the narrowbandness of the convolution filter h . All magnitude parameters were set one, see Fig. 4 for the width (Sinc) and lengthscales (SE).

5. The blind deconvolution case

(a) Training and observability

Implementing GPDC requires choosing the hyperparameters, i.e., the parameters of K_x and h , and the noise variance σ^2 . Depending on the application the filter might be known beforehand, for instance, in de-reverberation [42] h is given by the geometry of the room, whereas in astronomy h is given by the atmosphere and/or the telescope [43,44]. When h is unknown, a case referred to as *blind deconvolution*, its parameters have to be learnt from data alongside the other hyperparameters.

We fit the proposed model—see eqs. (2.1)–(2.3)—by maximising the log-likelihood

$$l(K_x, \sigma^2, h) = -\frac{n}{2} \log 2\pi - \frac{1}{2} \log \det K_{\mathbf{y}} - \frac{1}{2} \mathbf{y}^\top K_{\mathbf{y}}^{-1} \mathbf{y}, \quad (5.1)$$

where $K_{\mathbf{y}} = K_f(\mathbf{t}, \mathbf{t}) + \mathbf{I}_N$, with \mathbf{I}_N the identity matrix of size N , and the relationship between K_f and K_x follows from eq. (3.1). Therefore, K_x , h and σ^2 appear in l in eq. (5.1) through $K_{\mathbf{y}}$.

Maximum likelihood, however, might not recover all hyperparameters in a unique manner, since h and K_x are *entangled* in $K_{\mathbf{y}}$ and thus can be unidentifiable. For instance, if both h and K_x are SEs (as in Example 1) with lengthscales l_h and l_x respectively, then $K_{\mathbf{y}}$ is also an SE with lengthscales $l_y = l_x + l_h$; therefore, the original lengthscales cannot be recovered from the learnt l_y . More intuitively, the unobservability of the convolution can be understood as follows: a given signal f could have been generated either i) by a fast source x and a wide filter h , or ii) by a slow source and a narrow filter. Additionally, it is impossible to identify the temporal location of h only from \mathbf{y} , since the likelihood is insensitive to time shifts of x and h . Due to the symmetries in the deconvolution problem learning the hyperparameters should be aided with as much information as possible about h and K_x , in particular in the *blind* scenario.

(b) A tractable approximation of h

Closed-form implementation of GPDC *only* depends on successful computation of the integrals in eqs. (3.1) and (3.3). Those integrals can be calculated analytically for some choices of K_x and h , such as the SE or Sinc kernels in Definitions 1 and 3 respectively, but are in general intractable. Though it can be argued that computing these integrals might hinder the general applicability of GPDC, observe that when the filter h is given by a sum of Dirac deltas $\{w_i\}_{i=1}^M$ at locations $\{l_i\}_{i=1}^M$, i.e.,

$$h(t) = \sum_{i=1}^M w_i \delta_{l_i}(t), \quad (5.2)$$

the covariance K_f and the cross-covariance K_{fx} turn into summations of kernel evaluations:

$$K_f(t) = \sum_{i=1}^M \sum_{j=1}^M w_i w_j K_x(l_i - (l_j - t)) \quad (5.3)$$

$$K_{xf}(t_1, t_2) = K_{xf}(t_1 - t_2) = \sum_{i=1}^M w_i K_x(l_i - (t_1 - t_2)). \quad (5.4)$$

The discrete-time filter h is of interest in itself, mainly in the digital signal processing community, but it is also instrumental in approximating GPDC for general applicability. This is because when the integral forms in K_f , K_{xf} , in eqs. (3.1) and (3.3), cannot be calculated in closed-form, they can be approximated using different integration techniques such as quadrature methods, Monte Carlo or even importance sampling (see detailed approximations in the Appendix).

In terms of training (required for blind deconvolution) another advantage of the discrete-time filter is that its hyperparameters (weights $\{w_i\}_{i=1}^M$) do not become entangled into $K_{\mathbf{y}}$, but rather each of them appear bilinearly in it—see eq. (5.3). This does not imply that parameters are identifiable, yet it simplifies the optimisation due to the bilinear structure. Lastly, notice that since the sample approximations of $K_{\mathbf{y}}$ (e.g., using quadrature or Monte Carlo) are of low

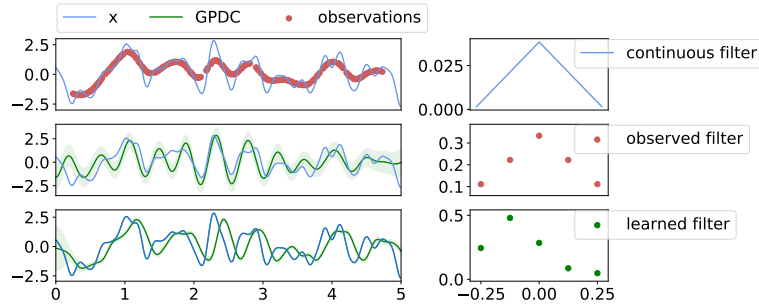


Figure 5: GPCD with a discrete-approximation filter h . Top: ground truth source x , observations \mathbf{y} and filter h . The ground truth x is drawn from a GP with a spectral mixture kernel K_x (see Def. 4) with parameters $\sigma = 1$, $\gamma = 50$, $\nu = 1$, $\sigma_n = 0.01$. Middle: GPDC (green) using a discrete filter calculated from the true h only K_x was learnt, our method recovered $\gamma = 11.8$, $\nu = 1.9$ and $\sigma_n = 0.03$ and the magnitude σ was fixed to one due to unobservability arising from the multiplication of h and K_x . Bottom: posterior deconvolution in the blind case: all hyperparameters, h , K_x and σ^2 , are learnt via maximum likelihood. The learnt filter is plotted in the bottom right corner (green dots) and the recovered parameters were $\gamma = 38.8$, $\nu = 1e^{-6}$ and $\sigma_n = 0.01$ (σ still fixed to one). Observe how, despite the seemingly poor recovery of the parameter values, the deconvolution in the blind case (bottom-left plot, green) was correctly detected only up to an unidentifiable temporal due to the unobservability issues mentioned above.

order compared with the data, they do not contribute with critical computational overhead, since evaluating eq. (5.1) is still dominated by the usual GP cost of $\mathcal{O}(N^3)$. Definitions 4 and 5 present the Spectral Mixture kernel and the triangular filter respectively, then Example 3 illustrates the discretisation procedure for training GPDC in the blind and non-blind cases as described above.

Definition 4. The stationary kernel defined as

$$K_{SM}(t) = \sigma^2 \exp\left(-\frac{1}{2l^2}t^2\right) \cos(2\pi\nu t) \quad (5.5)$$

is referred to as the (single component) Spectral Mixture (SM) and its parameters are magnitude σ , lengthscale l and frequency ν . Akin to the SE kernel in Def. 1, the SM kernel's lengthscale can be defined via its rate $\gamma = \frac{1}{2l^2}$. The Fourier transform of the SM kernel is an SE kernel centred in frequency ν .

Definition 5. The function defined as

$$h_{Tri}(t) = \sigma^2 \max\left(1 - \frac{2|t|}{\Delta}, 0\right) \quad (5.6)$$

is referred to as the triangular filter, also known as the Bartlett window, and its parameters are magnitude σ and width Δ .

Example 3. Let us consider the case where K_x is an SE kernel (see Def. 1) and h is a triangle (see Def. 5). We avoid computing the integrals for K_f and $K_{x,f}$, and consider two scenarios: i) learn discrete approximations both for h and K_x via maximum likelihood as in Sec. 5(a), ii) fix a discrete filter according to the true h , and only train K_x as in Sec. 5(b). Fig. 5 shows these implementations, notice how the discrete filter (only 5 points) allows for a reasonable recovery of the latent source x from \mathbf{y} . Furthermore, according to the unobservability of h , there is an unidentifiable lag between the true source and the deconvolution for the blind case.

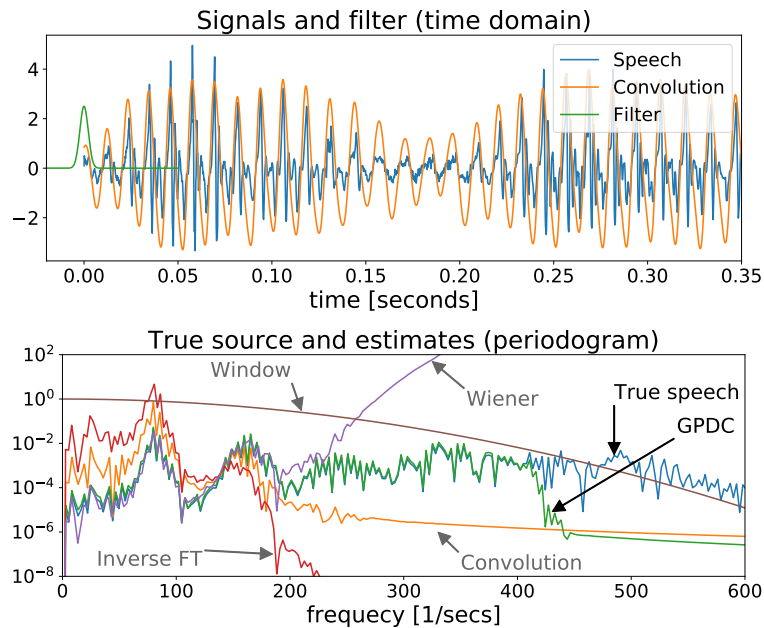


Figure 6: Recovering a speech signal using GPDC, Wiener and the Inverse FT method. Signals are shown in the temporal domain (top) and estimates in the frequency domain (bottom).

6. Experiments

We tested GPCD in two experimental settings. The first one simulated an acoustic de-reverberation setting and its objective was to validate the point estimates of GPDC in the noiseless, no-missing-data, case (i.e., $\sigma_n^2 = 0$) against standard deconvolution methods. The second experiment dealt with the recovery of latent images from low-resolution, noisy and partial observations, both when the filter h is known or unknown (a.k.a. blind superresolution). The code used for the following experiments and the examples in the paper can be found in <https://github.com/GAMES-UChile/Gaussian-Process-Deconvolution>.

(a) Acoustic deconvolution.

We considered a 350 [ms] speech signal (from <http://www.mcsquared.com/reverb.htm>), re-sampled at 5512.5 hertz (i.e., 2000 samples), standardised it and then convolved it against an SE filter of lengthscale $l = 2.2$ [ms]. Fig. 6 (top) shows the speech signal, the filter and the convolution. Since speech is known to be piece-wise stationary, we implemented GPDC using an SE kernel, then learnt the hyperparameters via maximum likelihood as explained in Section 5(a). The learnt hyperparameters were $\sigma = 0.95$, $l = 5 \cdot 10^{-4}$, $\sigma_{\text{noise}} = 0.12$. Notice that these values are consistent with the data pre-processing (the variances sum approximately one since the signal was standardised) and from what is observed in Fig. 6 (top) regarding the lengthscale.

The proposed GPDC convolution (assuming a known filter h given by an SE kernel presented above) was compared against the *Wiener* deconvolution and the *Inverse FT* methods mentioned in Sec. 2. Fig. 6 (bottom) shows the periodogram of the data alongside Wiener, Inverse FT and GPDC, and the filter h . Observe how GPCD faithfully followed the true latent source across most the spectral range considered, whereas Wiener diverged and the Inverse FT decayed rapidly perhaps due to their numerical instability. It is worth noting that the GPDC estimate ceases to follow the true source precisely at the frequency when the filter decays, this is in line with Thm. 1. Table 1 shows the performance of the methods considered in time and frequency, in particular via the discrepancy between the true power spectral density (PSD) and its estimate using the MSE, the KL

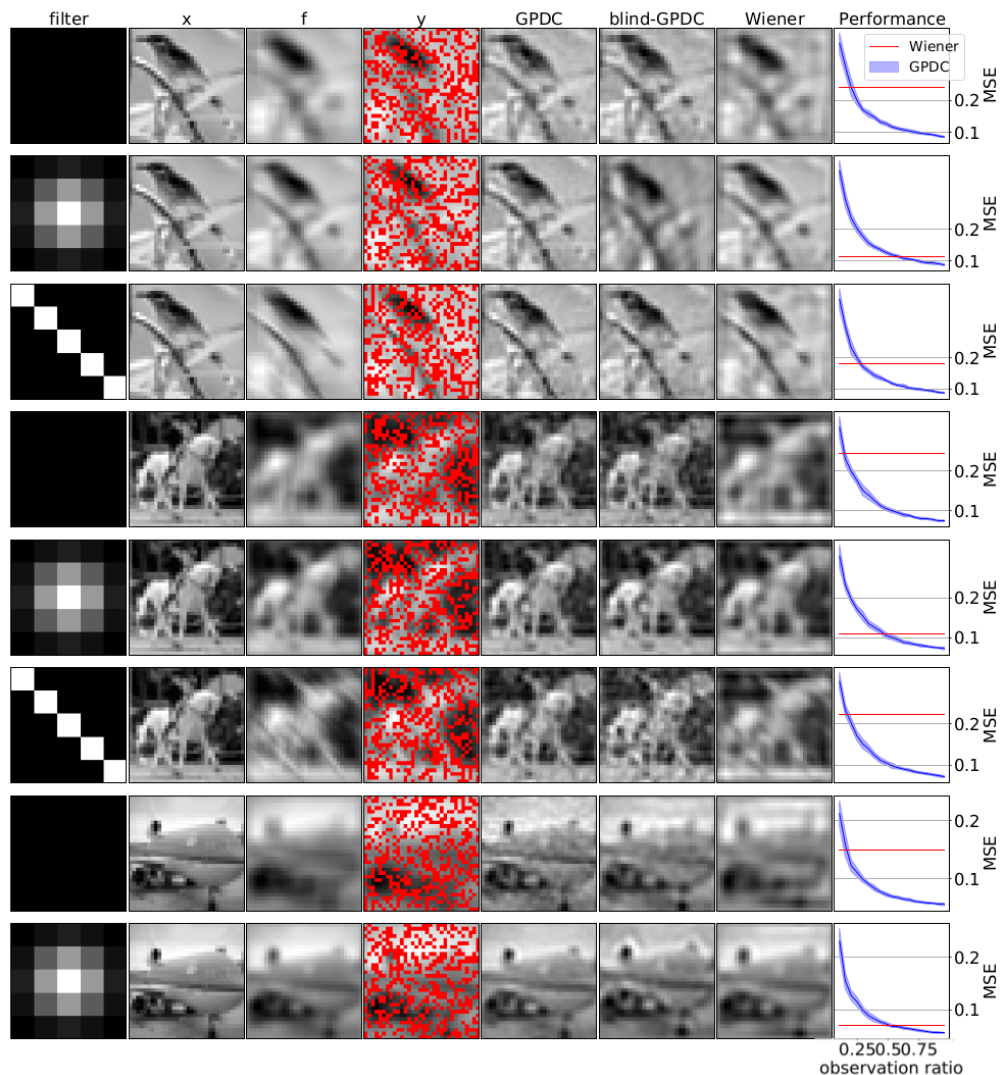


Figure 7: Deconvolution of 8 images from lower-resolution, noisy and incomplete observations. These 8 images were created from 3 source images to which we applied one of the five described filters. Left to right: filter used h , true image x , convolution f , observation y (25% missing pixels in red), GPDC estimate, blind-GPDC estimate and Wiener estimate. Rightmost plots show the performances of GPDC (blue) and Wiener filter (red) versus the number of observed pixels (2-standard-deviation error bars computed over 20 trials for GPDC).

divergence and Wasserstein distance [45] (the lower the better). Notice that GPDC outperformed Wiener and inverse FT under all metrics. The estimates in the temporal domain are shown in additional figures in the Appendix.

(b) Blind image super-resolution.

For a 32×32 image x , we created a convolved image f using a 5×5 filter h , and a noise-corrupted missing-data (60% of pixels retained) observation y . We implemented GPDC to recover x from y both when h is **known** and when it is **unknown**, therefore, for each image, we considered i) the case where the discrete filter h is known and used by GPDC, and ii) the case where h is learnt from

metric	GPDC	Wiener	inv-FT
MSE (time)	19.0	35.0	41.9
MSE (PSD)	0.015	0.058	0.153
Kullback–Leibler (PSD)	0.05	0.20	0.45
Wasserstein (PSD)	2124.3	3643.8	4662.6

Table 1: Quantitative evaluation of the audio de-reverberation experiment in time and frequency

data via maximum likelihood. We present results using three different filters: constant, unimodal and diagonal for the main body of the manuscript (Fig. 7), and other additional shapes in the Appendix. In all cases, we assumed an SE kernel for the source (ground truth image) and for each case we learnt the lengthscale l , the magnitude σ and the noise parameter σ_n . For the blind cases the discrete filter h was also learnt.

GPDC was compared against the Wiener filter (from `scikit-image`), applied to the **complete, noiseless**, image f . The reason to compare the proposed GPDC to the standard Wiener filter applied over the true image f instead of the generated observations \mathbf{y} is twofold: i) it serves as a benchmark that uses all the image information, and ii) the Wiener is unable to deal with missing data (as in \mathbf{y}) in its standard implementation. Fig. 7 shows the results for combinations of 3 different images from CIFAR-10 [46] and up to three different filters for each image. Notice how both non-blind and blind GPDC were able to provide reconstructions that are much more representative of the true image (x) than those provided by the Wiener filter. The superior performance of GPDC, against the Wiener benchmark, is measured through the mean squared error with respect to the true image x as a function of the amount of seen data (rightmost plot in Fig. 7). The Appendix includes additional examples with different images and filters.

7. Discussion and Conclusions

We have proposed Gaussian process deconvolution (GPDC), a methodology for Bayesian nonparametric deconvolution of continuous-time signals which builds on a GP prior over the latent source x and thus allows us to place error bars on the deconvolution estimate. We studied the direct generative model (the conditions under which it is well defined and how to sample from it), the inverse problem (we provided necessary conditions for the successful recovery of the source), the blind deconvolution case, and we also showed illustrative examples and experimental validation on dereverberation and super-resolution settings. A key point of our method in connection with the classical theory can be identified by analysing eq. (4.2) in the Fourier domain, where we can interpret GPDC as a nonparametric, missing-data-able, extension of the Wiener deconvolution. In this sense, the proposed method offers a GP interpretation to classic deconvolution, thus complementing the deconvolution toolbox with the abundant resources for GPs such as off-the-shelf covariance functions, sparse approximations, and a large body of dedicated software.

When constrained to the discrete and non-missing data scenario, our method reduces to the standard Wiener deconvolution, known in the literature [9]; thus, we have focused on comparing GPDC to the Wiener deconvolution method. However, despite the interpretation of GPDC from the viewpoint of classic deconvolution, we have considered a setting that is entirely different to that of digital communications. We have focused on estimating a continuous-time object (the source x) using a set of finite observations \mathbf{y} , which are to be understood as noise-corrupted and missing-part realisations of the convolution process $f = x \star h$, and to quantify the uncertainty of this estimate. Since we have limited information about the source (x can only be known through \mathbf{y} as per eq. (2.3)), we take a Bayesian approach and impose a prior over x , this prior is a Gaussian process. To the best of our knowledge, there is no prior work addressing this setting in conceptual

terms from a theoretical perspective, with the exception of a few works that have applied it to specific problems (see [31–35]).

As far as novel deconvolution methods are concerned, the trend in the literature is to merge neural networks with classical concepts such as prior design [20] and the Wiener filter [21], and are mainly applied to images, perhaps following the strong and steady advances in deep learning for computer vision. However, despite some recent applications of GPs to the deconvolution problem in particular settings, there are, to the best of our knowledge, no method addressing the recovery of a continuous-time (or continuous-space in the case of images) object from a finite number of noisy observations for both the blind and non-blind cases with the two main properties of our proposal: i) taking a Bayesian standpoint that allows for the determination of error bars, and ii) providing the Fourier-inspired guarantees in Sec. 4(a). In this sense, we claim that ours is the first application-agnostic study of the method which established the conditions for the proper definition of the hierarchical model, the capacity of the deconvolution procedure, and a principled quantification of uncertainty.

We hope that our findings pave the way for applications in different sciences and also motivates the GP community to consider extensions of our study. In particular, we envision further research efforts to be dedicated in the following directions:

- to develop sufficient (rather than only necessary) conditions for deconvolution to complement Theorem 1 and thus connecting with the interface between spectral estimation and GPs [47].
- to construct sparse GPs by controlling temporal correlation through trainable, multi-resolution, convolutions. This would provide computationally efficient sparse GPs with clear reconstructions guarantees.
- to develop a sparse GP version of the presented methodology in order to apply GPDC for deconvolution of large datasets

Data Accessibility. All data used in this article is either synthetic or public. Experiment 1 uses audio data from <http://www.mcsquared.com/reverb.htm>, while Experiment 2 uses CIFAR-10 [46].

Funding. We acknowledge financial support from Google and the following ANID-Chile grants: Fondecyt-Regular 1210606, the Advanced Center for Electrical and Electronic Engineering (Basal FB0008) and the Center for Mathematical Modeling (Basal FB210005).

References

1. Wang H, Sreejith S, Lin Y, Ramachandra N, Slosar A, Yoo S. 2022 Neural Network Based Point Spread Function Deconvolution For Astronomical Applications. *arXiv preprint arXiv:2210.01666*.
2. Clapp T, Godsill S. 1997 Bayesian blind deconvolution for mobile communications. In *IEE Colloquium Adaptive Signal Processing for Mobile Communication Systems (Ref. No. 1997/383)* pp. 9/1–9/6.
3. Willardson ML, Anderson BE, Young SM, Denison MH, Patchett BD. 2018 Time reversal focusing of high amplitude sound in a reverberation chamber. *The Journal of the Acoustical Society of America* **143**, 696–705.
4. Arya VK, Holden H. 1978 Deconvolution of seismic data—an overview. *IEEE Transactions on Geoscience Electronics* **16**, 95–98.
5. Hong H, Shi Y. 2017 Fast deconvolution for motion blur along the blurring paths. *Canadian Journal of Electrical and Computer Engineering* **40**, 266–274.
6. Tarantola A. 2005 *Inverse Problem Theory and Methods for Model Parameter Estimation*. SIAM.
7. Stuart AM. 2010 Inverse problems: A Bayesian perspective. *Acta Numerica* **19**, 451–559.
8. Aster RC, Borchers B, Thurber CH. 2018 *Parameter Estimation and Inverse Problems*. Elsevier.
9. Wiener N. 1964 *Extrapolation, Interpolation, and Smoothing of Stationary Time Series*. MIT Press.
10. Kalman RE. 1960 A new approach to linear filtering and prediction problems. *Journal of Basic Engineering* **82**, 35–45.
11. Riad S. 1986 The deconvolution problem: An overview. *Proceedings of the IEEE* **74**, 82–85.
12. Rasmussen C, Williams C. 2006 *Gaussian Processes for Machine Learning*. The MIT Press.

13. Bretthorst GL. 1992 Bayesian interpolation and deconvolution. Technical report Washington Univ St Louis Mo Dept Of Chemistry.
14. Rhode C, Whittenburg S. 1993 Bayesian Deconvolution. *Spectroscopy Letters* **26**, 1085–1102.
15. MacKay DJ. 2003 *Information theory, inference and learning algorithms*. Cambridge University Press.
16. Adami KZ. 2003 Variational methods in Bayesian deconvolution. *Statistical Problems in Particle Physics, Astrophysics and Cosmology* p. 143.
17. Babacan SD, Molina R, Katsaggelos AK. 2008 Variational Bayesian blind deconvolution using a total variation prior. *IEEE Transactions on Image Processing* **18**, 12–26.
18. Jeulin D, Renard D. 1992 Practical limits of the deconvolution of images by kriging. *Microscopy Microanalysis Microstructures* **3**, 333–361.
19. Goovaerts P. 2008 Kriging and semivariogram deconvolution in the presence of irregular geographical units. *Mathematical geosciences* **40**, 101–128.
20. Ren D, Zhang K, Wang Q, Hu Q, Zuo W. 2020 Neural blind deconvolution using deep priors. In *Proceedings of the IEEE/CVF Conference on Computer Vision and Pattern Recognition* pp. 3341–3350.
21. Dong J, Roth S, Schiele B. 2020 Deep Wiener deconvolution: Wiener meets deep learning for image deblurring. In Larochelle H, Ranzato M, Hadsell R, Balcan M, Lin H, editors, *Advances in Neural Information Processing Systems* vol. 33 pp. 1048–1059. Curran Associates, Inc.
22. Boyle P, Frean M. 2005 Dependent Gaussian processes. In Saul LK, Weiss Y, Bottou L, editors, *Advances in Neural Information Processing Systems 17*, pp. 217–224. MIT Press.
23. Álvarez M, Lawrence ND. 2009 Sparse convolved Gaussian processes for multi-output regression. In Koller D, Schuurmans D, Bengio Y, Bottou L, editors, *Advances in Neural Information Processing Systems 21*, pp. 57–64. Curran Associates, Inc.
24. Parra G, Tobar F. 2017 Spectral mixture kernels for multi-output Gaussian processes. In Guyon I, Luxburg UV, Bengio S, Wallach H, Fergus R, Vishwanathan S, Garnett R, editors, *Advances in Neural Information Processing Systems* vol. 30. Curran Associates, Inc.
25. Tobar F, Bui T, Turner R. 2015 Learning stationary time series using Gaussian processes with nonparametric kernels. In *Advances in Neural Information Processing Systems 28*, pp. 3501–3509. Curran Associates, Inc.
26. Bruinsma W. 2016 The generalised Gaussian convolution process model. Master's thesis Department of Engineering, University of Cambridge.
27. Wilson AG, Hu Z, Salakhutdinov R, Xing EP. 2016 Deep kernel learning. In Gretton A, Robert CC, editors, *Proceedings of the 19th International Conference on Artificial Intelligence and Statistics* vol. 51 *Proceedings of Machine Learning Research* pp. 370–378 Cadiz, Spain. PMLR.
28. van der Wilk M, Rasmussen CE, Hensman J. 2017 Convolutional Gaussian processes. In Guyon I, Luxburg UV, Bengio S, Wallach H, Fergus R, Vishwanathan S, Garnett R, editors, *Advances in Neural Information Processing Systems 30*, pp. 2849–2858. Curran Associates, Inc.
29. Walker I, Glocker B. 2019 Graph convolutional Gaussian processes. In Chaudhuri K, Salakhutdinov R, editors, *Proceedings of the 36th International Conference on Machine Learning* vol. 97 pp. 6495–6504 Long Beach, California, USA. PMLR.
30. Blomqvist K, Kaski S, Heinonen M. 2019 Deep convolutional Gaussian processes. In *Joint European Conference on Machine Learning and Knowledge Discovery in Databases* pp. 582–597. Springer.
31. Asensio Ramos A, Petit P. 2015 Bayesian least squares deconvolution. *Astronomy & Astrophysics* **583**, A51.
32. Tobar F, Rios G, Valdivia T, Guerrero P. 2017 Recovering latent signals from a mixture of measurements using a Gaussian process prior. *IEEE Signal Processing Letters* **24**, 231–235.
33. Arjas A, Roininen L, Sillanpää MJ, Hauptmann A. 2020 Blind hierarchical deconvolution. In *IEEE International Workshop on Machine Learning for Signal Processing* pp. 1–6.
34. Paciorek CJ, Schervish MJ. 2006 Spatial modelling using a new class of nonstationary covariance functions. *Environmetrics: The official journal of the International Environmetrics Society* **17**, 483–506.
35. Ross S, Arjas A, Virtanen II, Sillanpää MJ, Roininen L, Hauptmann A. 2022 Hierarchical deconvolution for incoherent scatter radar data. *Atmospheric Measurement Techniques* **15**, 3843–3857.
36. Boloix-Tortosa R, Murillo-Fuentes JJ, Payán-Somet FJ, Pérez-Cruz F. 2018 Complex Gaussian processes for regression. *IEEE Transactions on Neural Networks and Learning Systems* **29**, 5499–5511.

37. Ambrogioni L, Maris E. 2019 Complex-valued Gaussian process regression for time series analysis. *Signal Processing* **160**, 215 – 228.
38. Tobar F, Turner R. 2015 Modelling of complex signals using Gaussian processes. In *Proceedings of IEEE International Conference on Acoustics, Speech, and Signal Processing* pp. 2209–2213.
39. Shannon CE. 1949 Communication in the Presence of Noise. *Proceedings of the Institute of Radio Engineers* **37**, 10–21.
40. Nyquist H. 1928 Certain Topics in Telegraph Transmission Theory. *Transactions of the American Institute of Electrical Engineers* **47**, 617–644.
41. Tobar F. 2019 Band-limited Gaussian processes: The sinc kernel. In *Advances in Neural Information Processing Systems* **32**, pp. 12749–12759. Curran Associates, Inc.
42. Naylor PA, Gaubitch ND. 2010 *Speech dereverberation*. Springer Science & Business Media.
43. Starck JL, Pantin E, Murtagh F. 2002 Deconvolution in astronomy: A review. *Publications of the Astronomical Society of the Pacific* **114**, 1051.
44. Tobar F, Araya-Hernández L, Huijse P, Djurić PM. 2021 Bayesian reconstruction of Fourier pairs. *IEEE Transactions on Signal Processing* **69**, 73–87.
45. Cazelles E, Robert A, Tobar F. 2021 The Wasserstein-Fourier distance for stationary time series. *IEEE Transactions on Signal Processing* **69**, 709–721.
46. Krizhevsky A. 2009 Learning multiple layers of features from tiny images. Technical report University of Toronto.
47. Tobar F. 2018 Bayesian nonparametric spectral estimation. In Bengio S, Wallach H, Larochelle H, Grauman K, Cesa-Bianchi N, Garnett R, editors, *Advances in Neural Information Processing Systems* vol. 31. Curran Associates, Inc.

Appendix

This section contains the detailed calculation needed for Theorem 1, as well as detailed figures to the audio deconvolution experiment and more examples for the image deconvolution experiment.

(a) Extended proof of Lemma 1

Lemma 2. *If the convolution filter h and the covariance K_x are both integrable, then $K_f(t)$ is integrable.*

Proof. This follows in the same vein as the standard proof of integrability of the convolution between two functions with a slight modification, since the definition of $K_f(t)$ —eq. (5) in the article—comprises the composition of two convolutions rather than just one. Therefore, using Fubini Thm and the triangle inequality (twice), we have

$$\begin{aligned}
 \int_{\mathbb{R}} |K_f(t)| dt &= \int_{\mathbb{R}} \left| \int_{\mathbb{R}} h(\tau') \int_{\mathbb{R}} h(\tau) K_x(\tau - (\tau' - t)) d\tau d\tau' \right| dt && \text{[Fubini on eq. (5)]} \\
 &\leq \int_{\mathbb{R}} \int_{\mathbb{R}} |h(\tau')| \int_{\mathbb{R}} |h(\tau)| |K_x(\tau - (\tau' - t))| d\tau d\tau' dt && \text{[triangle ineq. twice]} \\
 &= \int_{\mathbb{R}} |h(\tau')| \int_{\mathbb{R}} |h(\tau)| \int_{\mathbb{R}} |K_x(\tau - (\tau' - t))| dt d\tau d\tau' && \text{[Fubini]} \\
 &= \|h\|_1 \|h\|_1 \|K_x\|_1 \\
 &< \infty. && \text{[} h, K_x \in L_1 \text{]}
 \end{aligned}$$

□

(b) Calculations for Theorem 1

$$\begin{aligned}
\mathbb{E}[\hat{x}_w(\xi)|\mathbf{y}] &= \mathbb{E}[\mathcal{F}\{x(t)w(t)\}|\mathbf{y}] \\
&= \mathcal{F}\{\mathbb{E}[x(t)|\mathbf{y}]w(t)\} \\
&= \mathcal{F}\left\{\left(m_x(t) + K_{xy}(t, \mathbf{t})K_y^{-1}(\mathbf{t})\mathbf{y}\right)w(t)\right\} \\
&= \left(m_x(t) + \mathcal{F}\{K_{xy}(t, \mathbf{t})\}K_y^{-1}(\mathbf{t})\mathbf{y}\right) \star \hat{w}(\xi) \\
&= \left(\hat{m}_x(\xi) + \hat{K}_{xy}(\xi)e^{-j2\pi\mathbf{t}\xi}K_y^{-1}(\mathbf{t})\mathbf{y}\right) \star \hat{w}(\xi) \\
&= \left(\hat{m}_x(\xi) + \hat{K}_x(\xi)\hat{h}(\xi)e^{-j2\pi\mathbf{t}\xi}K_y^{-1}(\mathbf{t})\mathbf{y}\right) \star \hat{w}(\xi)
\end{aligned} \tag{7.1}$$

$$\begin{aligned}
\mathbb{V}[\hat{x}_w(\xi)|\mathbf{y}] &= \mathbb{V}[\mathcal{F}\{x(t)w(t)\}|\mathbf{y}] \\
&= \mathbb{E}\left[\overline{\mathcal{F}\{x(t)w(t) - \mathbb{E}[x(t)w(t)|\mathbf{y}]\}}\mathcal{F}\{x(t)w(t) - \mathbb{E}[x(t)w(t)|\mathbf{y}]\}|\mathbf{y}\right] \\
[\text{lin. exp.}] &= \mathbb{E}\left[\overline{\mathcal{F}\{(x(t) - \mathbb{E}[x(t)|\mathbf{y}])w(t)\}}\mathcal{F}\{(x(t) - \mathbb{E}[x(t)|\mathbf{y}])w(t)\}}|\mathbf{y}\right] \\
[\text{conv. thm}] &= \mathbb{E}[\mathcal{F}\{(x(-t) - \mathbb{E}[x(-t)|\mathbf{y}])w(-t) \star (x(t) - \mathbb{E}[x(t)|\mathbf{y}])w(t)\}|\mathbf{y}] \\
[\text{def. conv.}] &= \mathbb{E}\left[\mathcal{F}\left\{\int (x(-\tau) - \mathbb{E}[x(-\tau)|\mathbf{y}])w(-\tau)(x(t-\tau) - \mathbb{E}[x(t-\tau)|\mathbf{y}])w(t-\tau)\right\}|\mathbf{y}\right] \\
[\text{lin. conv.}] &= \mathcal{F}\left\{\int w(-\tau)\mathbb{E}[(x(-\tau) - \mathbb{E}[x(-\tau)|\mathbf{y}])(x(t-\tau) - \mathbb{E}[x(t-\tau)|\mathbf{y}])|\mathbf{y}]w(t-\tau)\right\} \\
[\text{def. cov.}] &= \mathcal{F}\left\{\int w(-\tau)\mathbb{V}[x(-\tau), x(t-\tau)|\mathbf{y}]w(t-\tau)\right\} \\
[\text{def. cov}] &= \mathcal{F}\left\{\int \left(K_x(t) - K_{xy}(-\tau, \mathbf{t})K_y^{-1}K_{yx}(\mathbf{t}, t-\tau)\right)w(-\tau)w(t-\tau)d\tau\right\} \\
&= \hat{K}_x(\xi) \star |\hat{w}(\xi)|^2 - \mathcal{F}\left\{\int w(-\tau)K_{xy}(-\tau, \mathbf{t})K_y^{-1}K_{yx}(\mathbf{t}, t-\tau)w(t-\tau)d\tau\right\} \\
&= \hat{K}_x(\xi) \star |\hat{w}(\xi)|^2 - \overline{\mathcal{F}\{w(t)K_{xy}(t, \mathbf{t})\}}K_y^{-1}\mathcal{F}\{K_{yx}(\mathbf{t}, t)w(t)\} \\
&= \hat{K}_x(\xi) \star |\hat{w}(\xi)|^2 - \overline{\hat{w}(\xi) \star \hat{K}_x(\xi)\hat{h}(\xi)e^{-j2\pi\mathbf{t}\xi}}K_y^{-1}\hat{w}(\xi) \star \hat{K}_x(\xi)\hat{h}(\xi)e^{-j2\pi\mathbf{t}\xi} \\
&= \hat{K}_x(\xi) \star |\hat{w}(\xi)|^2 - \|\hat{w}(\xi) \star \hat{K}_x(\xi)\hat{h}(\xi)e^{-j2\pi\mathbf{t}\xi}\|_{K_y^{-1}}
\end{aligned} \tag{7.2}$$

(c) Extended audio experiment

For the audio de-reverberation experiment (see Fig. 6 in the main body of the article), we also show the estimates of all methods considered in detail. First, Fig. 8 shows the true signals (and filter), while Fig. 9 shows the estimate of the proposed GPDC (mean and 95% error bars). Figs. 10 and 11 show the estimates provided by the Wiener and Inverse FT methods respectively, considered as benchmarks to GPDC in this experiment. We also clarify that, as these last two methods perform direct deconvolution in the frequency domain, they do not maintain the phase of the signal and thus they need to be aligned with the true signal—we have aligned them for visualisation purposes.

Based on the estimates of the source x provided by the Inverse FT, Wiener and proposed GPDC (Figs. 11, 10 and 9 respectively), we can see how the worst reconstruction provided by the Inverse FT (which does not consider the fact that the source is stochastic). Then, the reconstruction provided by Wiener improves over the Inverse FT, since Wiener considers the dynamics of both the filter and the signal, however, it lacks a *likelihood model*, meaning that it is not able to discriminate between the (noisy) observations \mathbf{y} and the convolution f . Lastly, observe that the

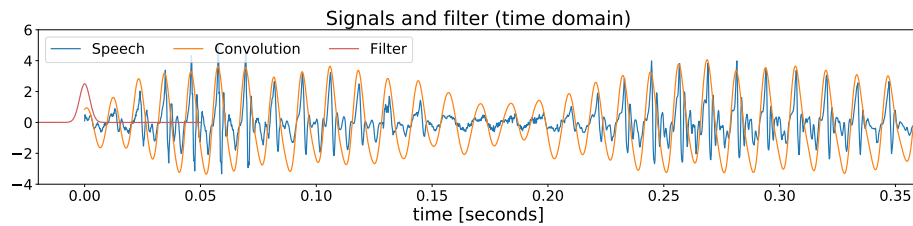


Figure 8: True audio signals (source and convolution) together with the convolution filter.

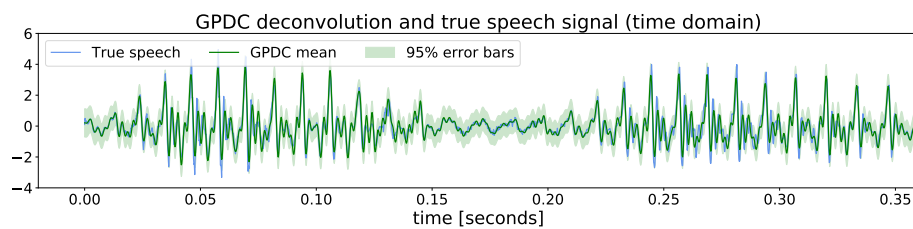


Figure 9: Deconvolution of a speech signal: GPDC estimate alongside true source and 95% error bars.

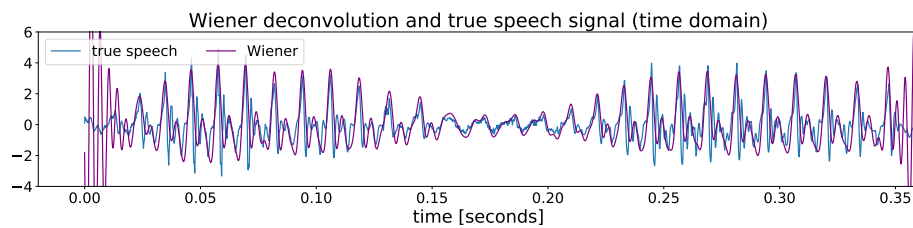


Figure 10: Deconvolution of a speech signal: Wiener estimate alongside true source.

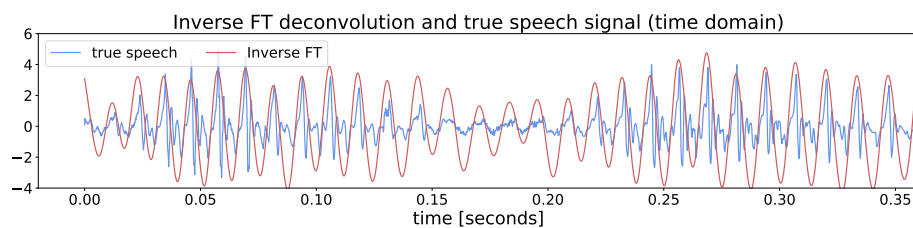


Figure 11: Deconvolution of a speech signal: Inverse FT estimate alongside true source.

proposed GPDC performed better than the benchmarks due to the fact that it incorporates both the dynamic behaviour of the source (through K_x) and the noise in the observations y .

(d) Extended image experiment

In this section, we include further simulations for the image deconvolution or *superresolution* experiments on additional test images and filters. This experiment aimed to validate the proposed GPDC and the blind GPDC (where the filter h is unknown and thus learnt from the images) against the Wiener deconvolution method. We considered the following (32×32) images from the CIFAR-10 Dataset: an airplane (Fig. 12), an emu (Fig. 13), a bird (Fig. 14), a horse (Fig. 15)

and a second airplane (Fig. 16). For all experiments, we considered 5 different filters h of size (5×5) pixels, these filters are shown in each figure from top to bottom colour-coded in grey scale between 0 and 1, and are given by:

- (i) h_0 : a constant filter,
- (ii) h_1 : a filter with a large (i.e., 1) at the origin and close to zero around the origin,
- (iii) h_2 : a radial filter that decays like a Gaussian RBF,
- (iv) h_3 : a filter composed of random values uniformly distributed between 0 and 1, and
- (v) h_4 : a diagonal filter.

Lastly, for all images and filters, GPDC and blind-GPDC were implemented with a number of observations ranging from 10% to 90% (for the performance plot), where the Figures exhibit the case for 30% missing data.

To understand the performance of the proposed GPDC and its blind variant against Wiener, recall that **the Wiener benchmark was implemented on the complete and noiseless image**, whereas the proposed model had access only to a missing-data and noisy version of the image. Let us observe that for the filters h_1 and h_2 , although the Wiener outperforms GPDC and blind-GPDC, the proposed models present a monotonic improvement wrt to the number of observations and even the blind GPDC is visually able to recover the true image. For more complex filters (h_0, h_2, h_4) we can see how both GPDC methods greatly outperform the Wiener benchmark whenever more than a 25% of the image is available. This behaviour is consistently found for all images, thus validating the robustness of the proposed GPDC methods while dealing with different images.

In all the following figures, the results are shown in the following order from left to right: filter (values between 0 and 1 colour-coded in grey scale), true image x , convolution f , observation y (30% missing pixels in red), GPDC estimate, blind-GPDC estimate, Wiener estimate and performance of GPDC versus amount of observed pixels (error bars for 20 trials). For each figure, each row is a realisation of the same experiment but with a different filter.

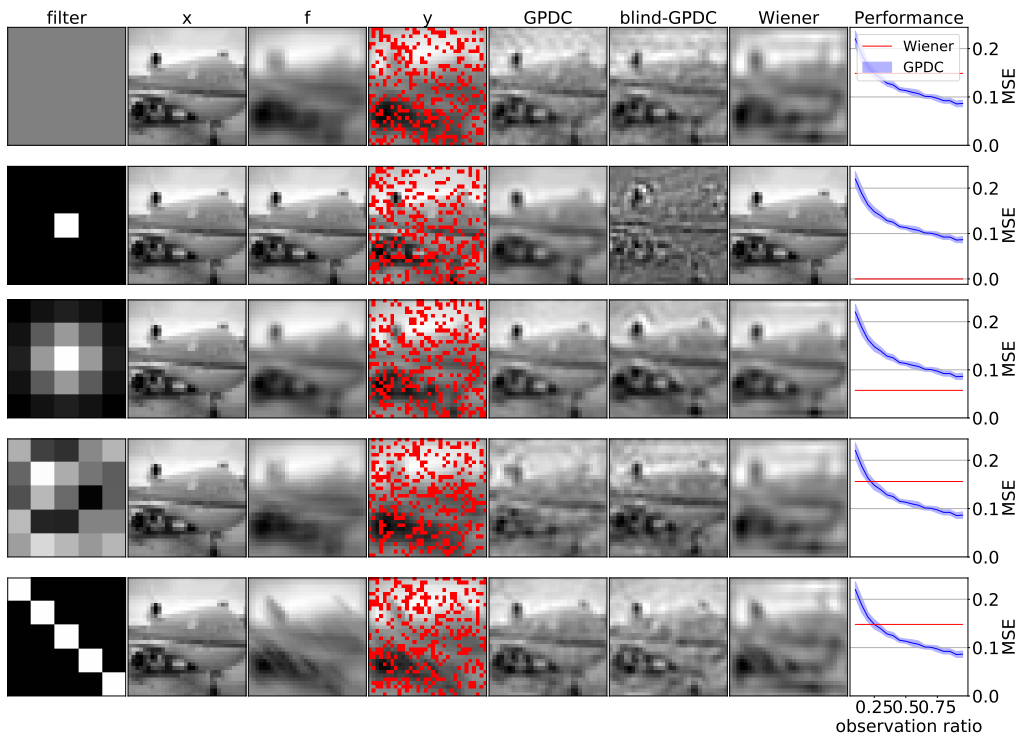


Figure 12: Picture of a plane.

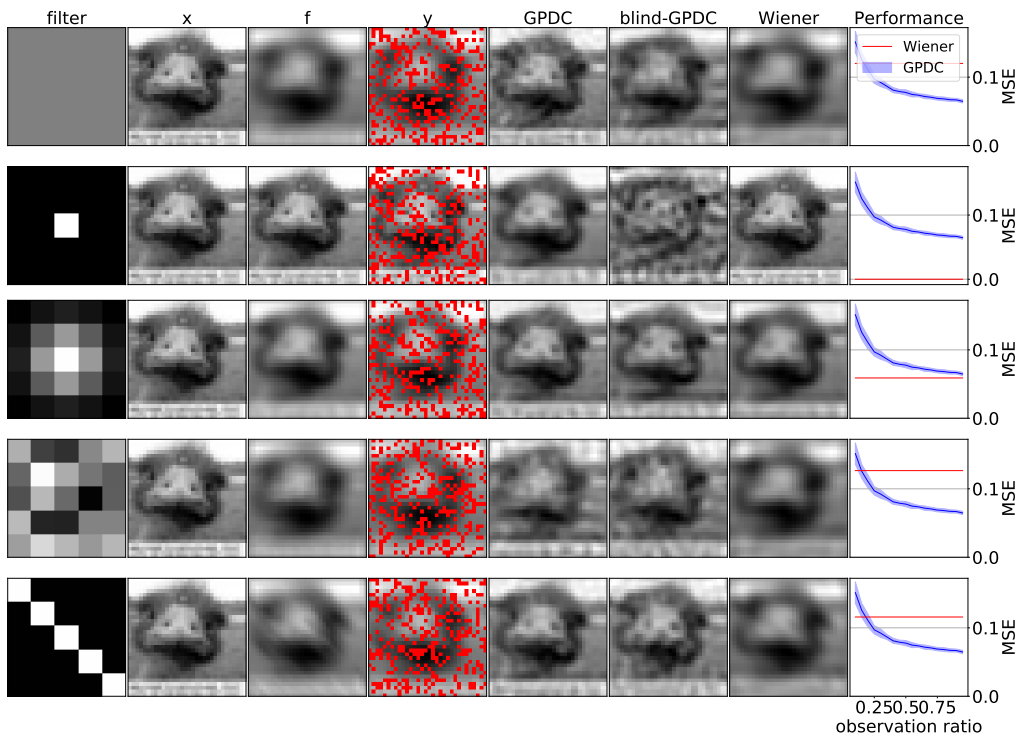


Figure 13: Picture of an Emu.

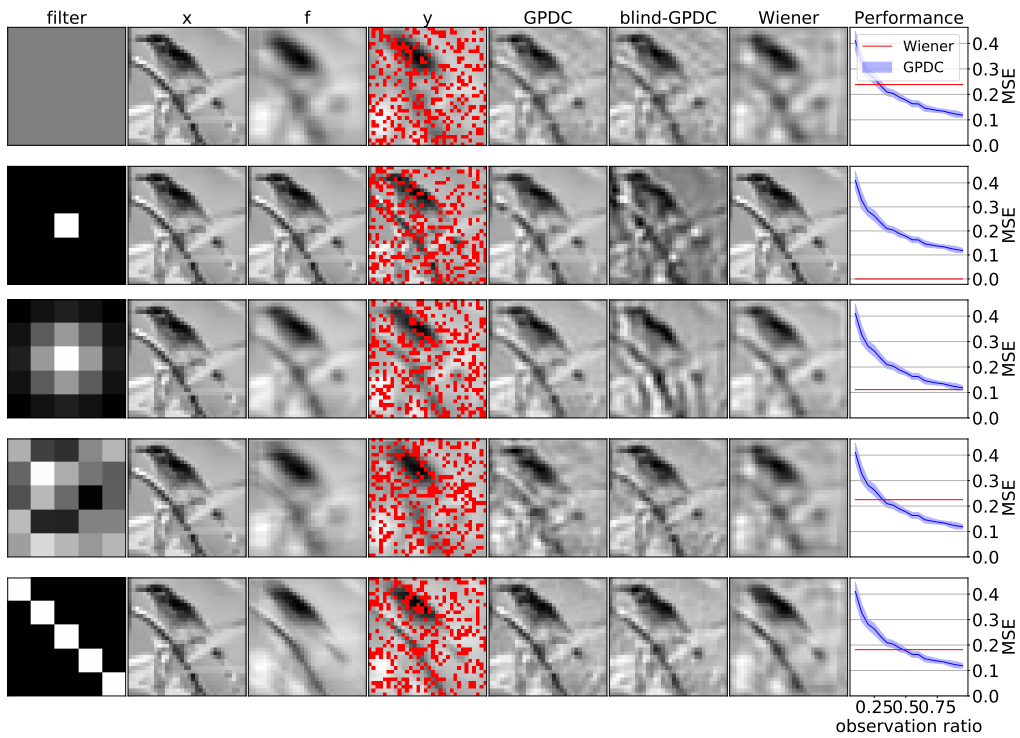


Figure 14: Picture of a bird.

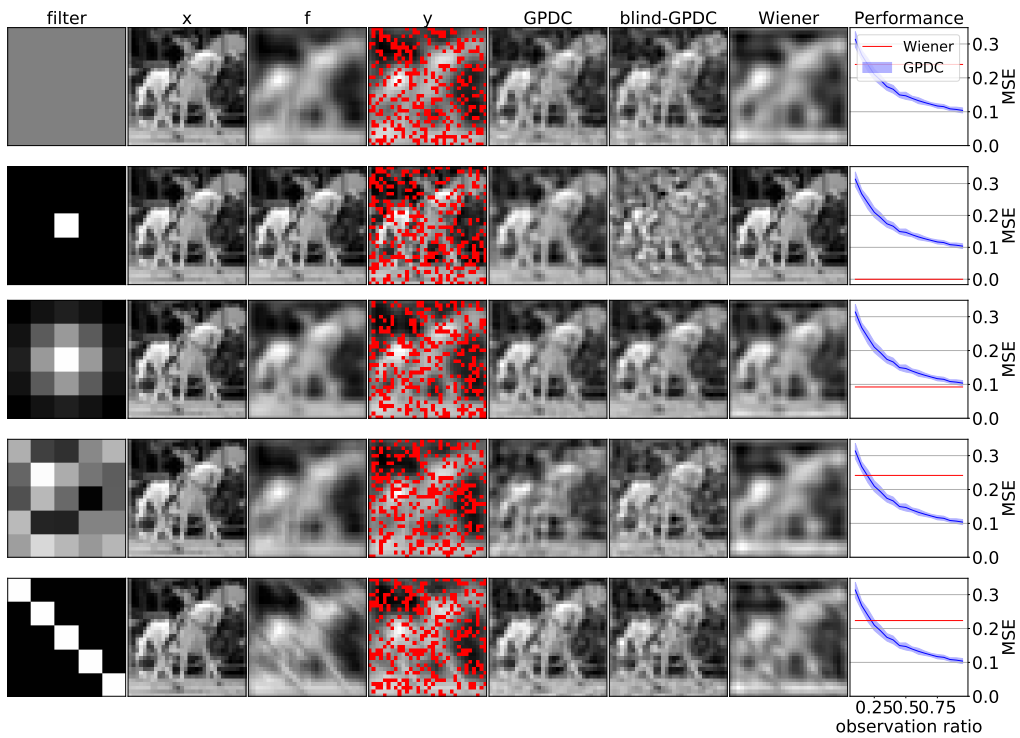


Figure 15: Picture of a horse.

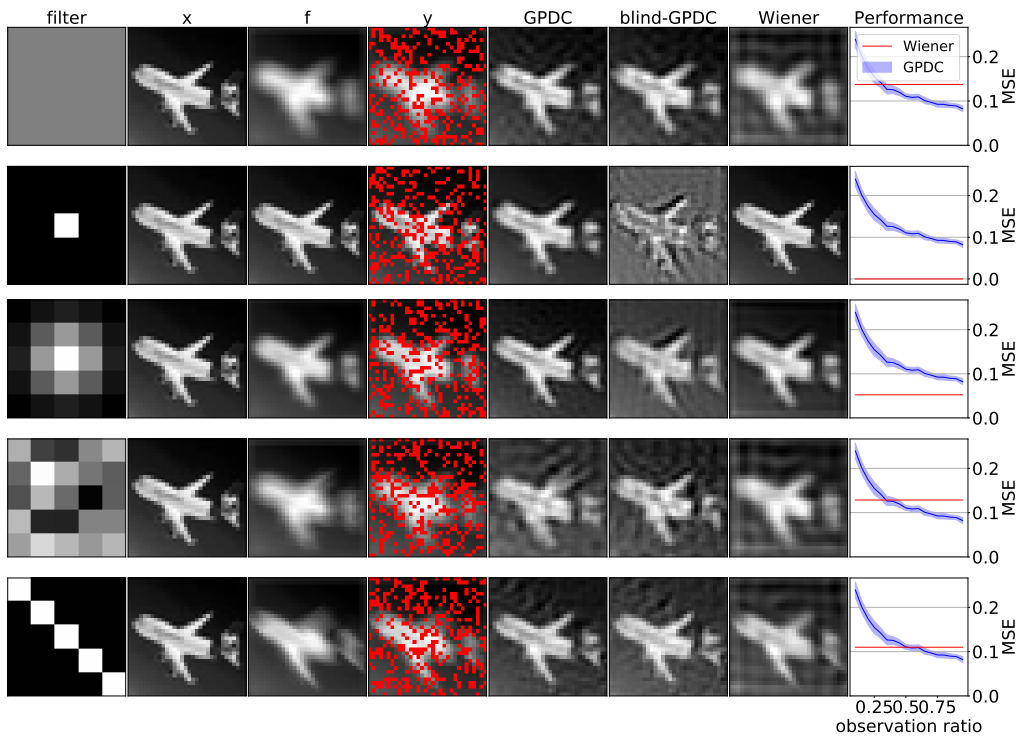


Figure 16: Second picture of a plane.